UC Irvine
UC Irvine Electronic Theses and Dissertations

Title

Thermal Transport Investigation of Nanograined Silicon Using Monte Carlo Ray Tracing and Molecular Dynamics Simulations

Permalink

https://escholarship.org/uc/item/3d769298

Author

Cao, Jiahui

Publication Date

2023

Peer reviewed|Thesis/dissertation

UNIVERSITY OF CALIFORNIA,
IRVINE

Thermal Transport Investigation of Nanograined Silicon Using Monte Carlo Ray Tracing
and Molecular Dynamics Simulations

THESIS

submitted in partial satisfaction of the requirements
for the degree of

MASTER OF SCIENCE

in Mechanical and Aerospace Engineering

by

Jiahui Cao

Thesis Committee:
Associate Professor Jaeho Lee, Chair
Assistant Professor Penghui Cao
Professor Yun Wang

2023

DEDICATION

To

my parents, family, and friends

in recognition of their love and support

TABLE OF CONTENTS

Page

LIST OF FIGURES

LIST OF TABLES

ACKNOWLEDGEMENTS

I would like to express the deepest appreciation to my committee chair, Professor Jaeho Lee, for his invaluable guidance, unwavering support, and remarkable mentorship throughout my graduate study at the University of California, Irvine (UCI). He introduced me to the fields of thermal science and thermoelectric since I was an undergraduate student at UCI. He constantly encourages me to think and act as a scholar and motivates me explore new areas and ideas. He supports me to collaborate with different groups, present my research at conferences, and reach out to national labs for internship opportunities. I would like to acknowledge his role in broadening my horizons within the fields. His extensive network and willingness to connect me with esteemed professionals, industry experts, and research collaborators have opened doors to invaluable experiences and collaborations. These opportunities have not only expanded my knowledge but have also allowed me to forge meaningful connections within the thermal science and thermoelectric community.

I would like to thank my committee member, Professor Penghui Cao, who also serves as a co-advisor for this collaborative project of nanograined silicon. He provides a lot of invaluable feedback to my manuscript preparation and helps me to address potential questions that could arise from the journal reviewers. I would also like thank my committee member, Professor Yun Wang. Professor Wang is very knowledgeable in the field of multiphase flow, fuel cells, and transport phenomena. I am still very impressed by the questions and advice given to me when I presented my final project in his Advanced Transport Phenomena course.

I would like to acknowledge my collaborators, Han Wang, for his input in the Molecular Dynamics simulations on the mechanical properties of nanograined silicon, and Dr. Laia Ferrer-Argemi, for the groundwork that is significant to the work presented in this thesis. I also want to extend my appreciation to Dr. Zongqing Ren, Dr. Xiao Nie, Jungyun Lim, Hoyeon Park, Jiajian Luo, and Charles Owens for their friendship, interactions, and advice in various research projects.

Most importantly, I would like to thank my family for their unconditional love, support, and encouragement for my graduate study as a first-generation student. They support me to overcome challenges, encourage me to improve myself, and share all the pressures and joys with me. I dedicate this master thesis to them!

ABSTRACT OF THE THESIS

Thermal Transport Investigation of Nanograined Silicon Using Monte Carlo Ray Tracing
and Molecular Dynamics Simulations

by

Jiahui Cao

Master of Science in Mechanical and Aerospace Engineering

University of California, Irvine, 2023

Professor Jaeho Lee, Chair

Nanocrystalline silicon can have unique thermal transport and mechanical properties governed by the constituent grain microstructure. In this thesis work, we use phonon ray-tracing and molecular dynamics simulations to demonstrate the largely tunable thermomechanical behaviors with varying grain sizes (a_0) and aspect ratios (ξ). We show that by selectively increasing the grain size along the heat transfer direction while keeping the grain area constant, the in-plane thermal conductivity (k_x) increases more significantly than the cross-plane thermal conductivity (k_y), originating from anisotropic phonon-grain boundary scattering. The k_x increases with increasing aspect ratio ξ until a critical value, at which k_x reaches a maximum. Further increase in ξ leads to a decrease in k_x, steaming from substantial scattering of low-frequency phonon with anisotropic grain boundaries. In addition, we find the elastic modulus shows strong size-dependence, and the softening effect leads to significant reductions in the phonon group velocity and the thermal conductivity. By accounting for both thermal and mechanical size effects, we identify two distinct regimes of thermal transport, in which anisotropic phonon-grain boundary scattering becomes more appreciable at low temperatures and phonon softening becomes more appreciable at high

temperatures. Through spectral analysis, we attribute the significant thermal conductivity anisotropy in the nanocrystalline silicon to grain boundary scattering of low-frequency phonons and the softening-driven thermal conductivity reductions to Umklapp scattering of high-frequency phonons. These findings suggest new pathways to manipulate thermomechanical properties of nanocrystalline silicon via microstructure engineering, having profound implication for future anisotropic nanomaterials.

CHAPTER 1: INTRODUCTION

1.1 Thermal Size Effect and Mechanical Size Effect in Silicon Nanostructures

Nanostructuring has been proven to be a reliable approach to reducing silicon's intrinsic high thermal conductivity, originating from substantial phonon-boundary scattering with feature sizes scaling below the phonon mean free path and even comparable to the phonon wavelength [1], [2]. Experimental work on polysilicon [3], [4] and Si nanoporous structures [5]–[8] has shown lattice thermal conductivity reductions beyond classical models (e.g., due to phonon ballistic thermal transport [7] or thermally dead volume[8]). Unlike nanowires [2], [9], nanomeshes [10], [11], and nanoribbons [8], [12], of which the phonon-boundary scattering strongly depends on some simple geometric parameters such as the diameters of nanowires, the pitch and neck sizes of nanomeshes, and the backbone and fin dimensions of nanoribbons, the understanding of phonon-boundary scattering with grain boundaries and its frequency dependent nature is still incomplete and requires further investigations. On the other hand, reducing the material size to a nano regime can significantly influence mechanical behaviors. Known as "smaller is stronger," the strength of polycrystalline metals tends to increase as the grain size decreases [13]. However, when the grain size reaches a critical value (∼ 20 nm) [14]–[16], softening will take over. This is governed by the transition of deformation mechanism from dislocation-mediated plasticity to grain-boundary-mediated deformation [17]. Studies have also shown a dependence of microhardness and elastic modulus on the grain size of nanocrystalline silicon [18]–[20]. Moreover, by studying the deformation mechanism of single-crystalline and polycrystalline silicon, it has been found that the grain boundaries existing in

polycrystalline silicon can serve as preferential sites for high-pressure phase transformation and provide a deformation mechanism dissimilar to single-crystalline silicon [21]. As a result, it is reasonable to speculate that grain boundaries could play a more crucial role while reducing grain size to nano regime and contributing to both the mechanical and thermal properties of nanograined silicon.

1.2 Lattice Softening Effect and Thermal Transport in Nanomaterials

In nanostructures, reduced thermal conductivity is usually attributed to a reduced mean free path arising from boundary scattering, Λ_B. In contrast, phonon/lattice softening causes an additional reduction in the thermal conductivity of nanostructures that arises from a reduction in the phonon group velocity [22]. From a microscopic point of view, phonon scattering and lattice softening effects arise from the interactions of propagating phonon wave packets with the material's internal-strain fields, which are induced by lattice defects such as dislocations and nanoprecipitates. These internal-strain fields can locally change phonon frequencies within the material and can, in principle, lead to lattice softening [23]. In other words, lattice softening refers to a decrease in the phonon speed or the magnitude of the group velocity vector, and phonon scattering refers to a change in the direction of the phonon velocity vector while the phonon speed remains unchanged [23].
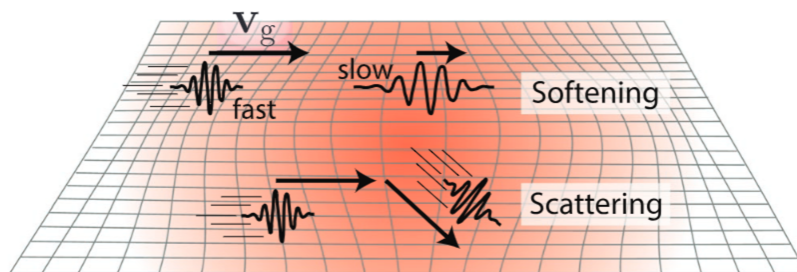
Figure 1.1 | Illustration of phonon scattering and lattice softening effects due to internal-strain fields. Image adapted from [23].

In practice, the change in speed of sound can be used as an estimate for the change in average phonon group velocity, $\langle v_g \rangle^3 \propto v_s^3$. In the continuum limit, the speed of sound, $v_s = \sqrt{E/\rho}$, is proportional to $\sqrt{E}$, where E is Young's modulus, implying that a softening of the material should induce a reduction in the phonon group velocity. Therefore, if the speed of sound (i.e. lattice stiffness) can be engineered in a material, it is expected to be an effective parameter for controlling the thermal conductivity. In the case of nanograined silicon, the mechanical strength and hence the thermal conductivity can be effectively engineered by selectively controlling the average grain size of the nanopowder/nanoparticles that will be subsequently consolidated by spark plasma sintering (SPS) [24]. Moreover, tuning the lattice stiffness is expected to have a more significant impact on lattice thermal conductivity, k_L, than micro/nanostructural scattering in some cases. For instance, at the high temperatures limit ($T \gg \theta_D$) where phonon–phonon scattering dominates ($\tau \approx \tau_{pp}$), the lattice thermal conductivity can be approximated as:

$$k_L = \frac{(6\pi^2)^{2/3} \overline{M}}{V^{2/3} 4\pi^2 \mu^2} \cdot \frac{\langle v_g^3 \rangle}{T} = A \frac{v_s^3}{T} \propto v_s^3 \tag{1}$$

where $\overline{M}$ and V are the average atomic mass and volume, respectively, and μ is the Grüneisen parameter [23]. Hence, the lattice thermal conductivity at the high temperatures limit is expected to reduce by a factor of 8 if the speed of sound (i.e. lattice stiffness) of the material is reduced by half. In the case of nanocrystalline silicon, as the effective grain size decreases to 4 nm, the elastic modulus decreases by 28.3% compared to the bulk value of 130 GPa [25], leading to a 39.3% reduction in k_L as predicted by equation (1).

1.3 Literature Review on Phonon-Grain Boundary Scattering

Several analytical and simulation models exist to account for phonon scattering with grain boundaries. The first studies just used the average grain size as a mean free path or a gray model [26]–[28]. However, experimental data indicates that the phonon scattering with grain boundaries is frequency-dependent [3], [29]. Atomistic simulations [30] and experimental transmission coefficient measurements [31] also suggest that the phonons' transmission probability sharply decreases with phonon frequency. Another crucial factor in these studies is the treatment of the phonons that cross the interface. Most theoretical studies on polysilicon have used Monte Carlo Ray Tracing (MCRT) simulations that assumed diffuse reflection or transmission at the grain boundaries [4], [32], but Hua and Minnich [33] define a specularity parameter for both reflected and transmitted phonons, and Chakraborty *et al.* [34] consider a completely specular transmission. Since only Hua and Minnich validate their modeling with one experimental data set, more investigation is needed on the comparison between the different phonon treatments at the grain boundary interface. Moreover, MCRT simulations are very computationally expensive and usually contain geometric scales smaller than the average mean free path [35]. Thus, there is no work studying the effect of the orientation of the grain boundaries nor the effect of anisotropic grain boundaries. However, new materials with interesting grain structures have recently emerged, such as nanograined diamond films with triangular hierarchical grains and nanowire-based pallets with greatly elongated grains [36], [37]. This motivates us to develop new analytical and simulation models to study both the thermal and mechanical properties of such structures.

In this thesis work, we establish a modeling framework that utilizes heat-flux driven Monte Carlo ray tracing (MCRT) to examine phonon scattering with grain boundaries. We validate the model by comparing the frequency-dependent treatments at the grain boundaries to experimental data [3]. Then we study the effect of grain anisotropy on phonon-boundary scattering mean free paths (Λ_{GB}) and evaluate their contribution to the thermal conductivity and thermal anisotropy of nanograined silicon over a wide temperature range. On the other hand, we use the Large-scale Atomic/Molecular Massively Parallel Simulator (LAMMPS) to investigate the mechanical behavior of nanograined silicon with designed grain heterogeneity that resembles a real grain structure. We study both the mechanical size effect and the effect of grain anisotropy on the elastic modulus and shear modulus. Correspondingly, we identify the critical grain size for lattice softening to take effect (i.e. the critical grain size of which the mechanical properties of nanograined silicon deviate from the bulk properties of silicon) and deduce the different thermal transport regimes for nanocrystalline silicon. Using the simulated elastic moduli and shear moduli and their relationship to the speed of sound, we further modify the Born-von-Karman (BvK) dispersion relation for bulk silicon to account for the lattice softening effect on the thermal conductivity of nanograined silicon. This thesis work represents a significant advancement in the understanding of phonon transport and serves as a valuable guide for optimizing grain structure engineering.

CHAPTER 2: MODELING, SIMULATION, AND METHODOLOGY

2.1 Thermal Conductivity Modeling

The Boltzmann transport equation (BTE) particle model for thermal conductivity under the common isotropic dispersion approximation is

$$k = \frac{GL}{A} = \frac{1}{3} \int c_v v_g \Lambda_{\text{eff}} \, d\omega \tag{2}$$

where G is the thermal conductance, L is the length, A is the cross-sectional area, C_v is the volumetric heat capacity, v_g is the phonon group velocity, and ω is the phonon angular frequency. We use the triply-degenerate isotropic Born-von-Karman sine-type dispersion to calculate the group velocity [38]. We also use the Matthiessen's rule under relaxation time approximation to obtain the effective mean free path, $\Lambda_{\text{eff}}^{-1} = \Lambda_B^{-1} + \Lambda_I^{-1} + \Lambda_U^{-1}$, that combines the contributions of boundary, impurity and defects, and Umklapp scatterings. The mean free paths for impurity and Umklapp scatterings have been well-studied for silicon [39], [40]. For impurity scattering, we use a Rayleigh-like expression [40], $\Lambda_I^{-1} = C_I \omega^4 / v_g$, where $C_I = 2.54 \times 10^{-45} \text{ s}^3$. For Umklapp scattering, we follow a common form, $\Lambda_U^{-1} = P\omega^2 T \exp\left(-\frac{C_U}{T}\right) / v_g$, where $P = 1.53 \times 10^{-19} \frac{\text{S}}{\text{K}}$ and $C_U = 144 \text{ K}$. Although there exist several analytical and simulation models for the phonon-grain boundary scattering mean free path (Λ_{GB}) of nanocrystalline silicon with uniform grain structure [3], [26], [33], Λ_{GB} is generally unknown for anisotropic grain structures with an aspect ratio (ξ) other than one. To rigorously determine the frequency-dependent Λ_{GB}, we combine Monte-Carlo ray tracing (MCRT) simulations with an atomistic relation for grain boundary transmission. One of the unique advantages of MCRT is that it can account for multi-dimensional phonon-boundary

scattering, allowing us to capture the impact of vertical and horizontal grain sizes on Λ_{GB} and investigate the thermal anisotropy induced by the anisotropic grain boundaries network.

2.2 Monte-Carlo Ray Tracing (MCRT) Framework
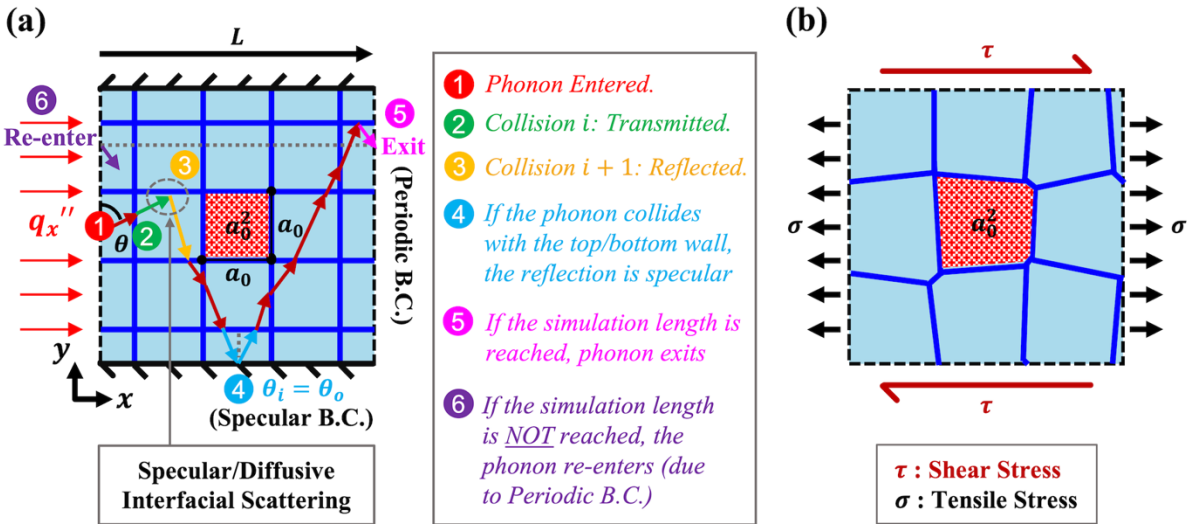
Figure 2.1 | Schematics of the Simulated Nanograined Si Geometry. (a) Ray Tracing simulation domain showing a typical phonon trajectory and various phonons interactions with grain boundaries and system domain boundaries. The unit cell has a specular boundary condition on the top and bottom walls and a periodic boundary condition on the left and right surfaces to periodically repeat itself until a simulation length, L, is reached. The length of the simulation domain is chosen by increasing L until the change in the calculated phonon-boundary mean free path is negligible, as it saturates to the diffuse limit. **(b)** Molecular dynamic simulation domain showing stresses applied for shear (red) and tension (black) deformation to derive elastic moduli. Note: we introduce a small degree of heterogeneity on grain boundaries in the molecular dynamic simulation domain to ensure that the simulated grain structure is mechanically stable at the corner. This slight modification will have little effect on the elastic and shear moduli compared to a homogenous structure that was used in the ray tracing simulation because the moduli of nanograined silicon are strongly influenced by the average grain size and grain anisotropy (see Chapter 3 for the result).

In our MCRT framework, as illustrated in **Figure 2.1(a)**, a large number of incident phonons are injected on the left wall of a semi-periodic and semi-specular unit cell with a trajectory probability that follows a normal distribution with the heat flux direction being

the mean. The trajectory of each phonon is tracked throughout the entire simulation domain – where the collisions with grain boundaries can be diffusive or specular – until the phonon reaches the end of the simulation domain (at $x = L$) or returns to the injection wall (at $x = 0$). We define the average transmission coefficient $\langle \mathcal{T} \rangle$ as the ratio of the number of fully transmitted phonons to the total number of injected phonons. Within the simulation domain, we generate a random number (between 0 and 1) once a collision with a grain boundary occurs; the phonon is reflected if this number is larger than grain boundary transmission probability (τ_{GB}) and it is transmitted if the number is smaller than τ_{GB}.
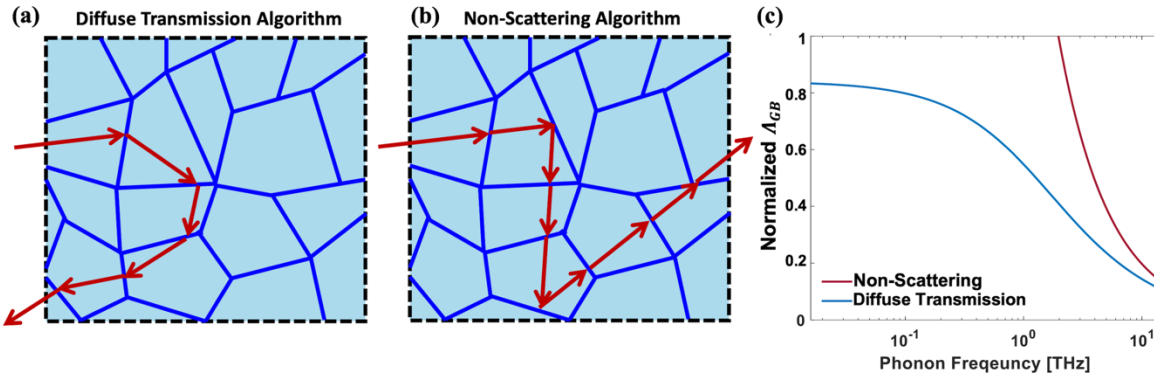
Figure 2.2 | Schematics of (a) diffuse and (b) non-scattering grain boundary transmission algorithms, and (c) their resulting phonon mean free path as a function of the phonon frequency. Diffuse transmission results in a trend that differs from the analytical expression proposed by Wang et al. [3] since a finite Λ_{GB} is reached for low frequency phonons.

The treatment of phonons across the interface/grain boundary is critical for analytical formulation of frequency-dependent Λ_{GB} for low frequency phonons. In fact, phonons that collide with a grain boundary and get transmitted would still have their direction affected by diffusive scattering (diffuse transmission algorithm), resulting in phonons not reaching the end of the simulation length even with a transmission probability at the boundaries of one as shown on **Figure 2.2(a)**. This phenomenon results in a finite Λ_{GB}

for low frequency phonons at a given grain structure, which differs from the analytical formulations available in the literature that estimate an infinite Λ_{GB} for low frequency phonons. This gives rise to a frequency independent scattering rate as showed by Klemens that is typically very small because the change in phonon velocity when crossing an interface is less than 10% [41]. However, the two boundaries of the intergrain region should be far apart compared to the phonon wavelength for scattering to be incoherent, suggesting the existence of a critical frequency below which scattering is increasingly coherent such as

$$\omega_{cr} \cong v/t \tag{3}$$

where v is the phonon velocity and t is the thickness of the intergrain region. The two boundaries would scatter phonons coherently when $\omega < \omega_{cr}$, which especially likely at low temperatures since t is typically ~ 5 Å [42] and the phonon frequencies are much smaller than ω_{cr}. Thus, for the purposes of our study, we impose the non-scattering algorithm such that phonons transmitted through the grain boundary can be scattered to be able to achieve an infinite Λ_{GB} at low frequencies as seen in **Figure 2.2(c).** This behavior is also consistent with the findings by Chen *et al*. in silicon-germanium alloys [43].

2.3 Frequency-Dependent Mean Free Path for Phonon-Grain Boundary Scattering

From the Landauer formalism [44], [45], the thermal conductance G defined in terms of a phonon transmission function $\mathcal{T}(\Omega, \omega)$ is

$$G = \frac{A}{4} \int C_v \langle \mathcal{T} \rangle v_g d\omega \tag{4}$$

where Ω is the solid angle, and the average transmission coefficient, $\langle \mathcal{T} \rangle = \frac{1}{\pi A} \int_0^{2\pi} \int_0^{\pi/2} \tau(\theta, \phi, A) \cos(\theta) \sin(\theta) d\theta d\phi dA$, can be obtained using ray tracing simulations

with Monte-Carlo integration, where θ and ϕ denote the polar angle and the azimuthal angle, respectively. Comparing the Landauer formulism (eq. 4) and the BTE model for thermal conductivity (eq. 2), we obtain an equation that relates the phonon mean free path, Λ, with the simulation length, L, and the average transmission coefficient:

$$\frac{\Lambda}{L} = \frac{3}{4} \langle \mathcal{T} \rangle \tag{5}$$

A characteristic behavior of diffusive transport is a mean free path Λ that saturates for long simulation length, L. The mean free path Λ calculated from the transmission coefficient $\langle \tau \rangle$ describes the combined effects of diffusive boundary scattering and a length-independent ballistic resistance (which can be represented through a transmission coefficient τ_{ball}) that depends on the configuration of the device-contact connection [11]. Due to the nature of grain boundary scattering, the simulation does not converge even at large simulation lengths for large transmission probabilities (see **Figure 2.3(a)**). To find the intrinsic Λ_{GB}, defined as $\lim_{L \to \infty} (\Lambda)$, from finite-$L$ simulations, we follow the technique of previous works [11], [46] and sum the ballistic and diffusive scattering in parallel in a Matthiessen's rule-type approximation, resulting in

$$\frac{L}{\Lambda} = \frac{1}{\tau_{ball}} + \frac{L}{\Lambda_{GB}} \tag{6}$$

As shown on **Figure 2.3(a)(b)**, we first calculate Λ for a square grain structure ($\xi = 1$ and $a_0 = 100\,nm$) as a function of L and then use a linear regression fitting to eq. (6) to determine the saturated Λ_{GB} for various grain boundary transmission probabilities, $\tau_{GB} \in [0.1, 0.2, 0.3, 0.4, 0.5, 0.6, 0.7, 0.8, 0.9, 0.95]$.

(a)

(b)
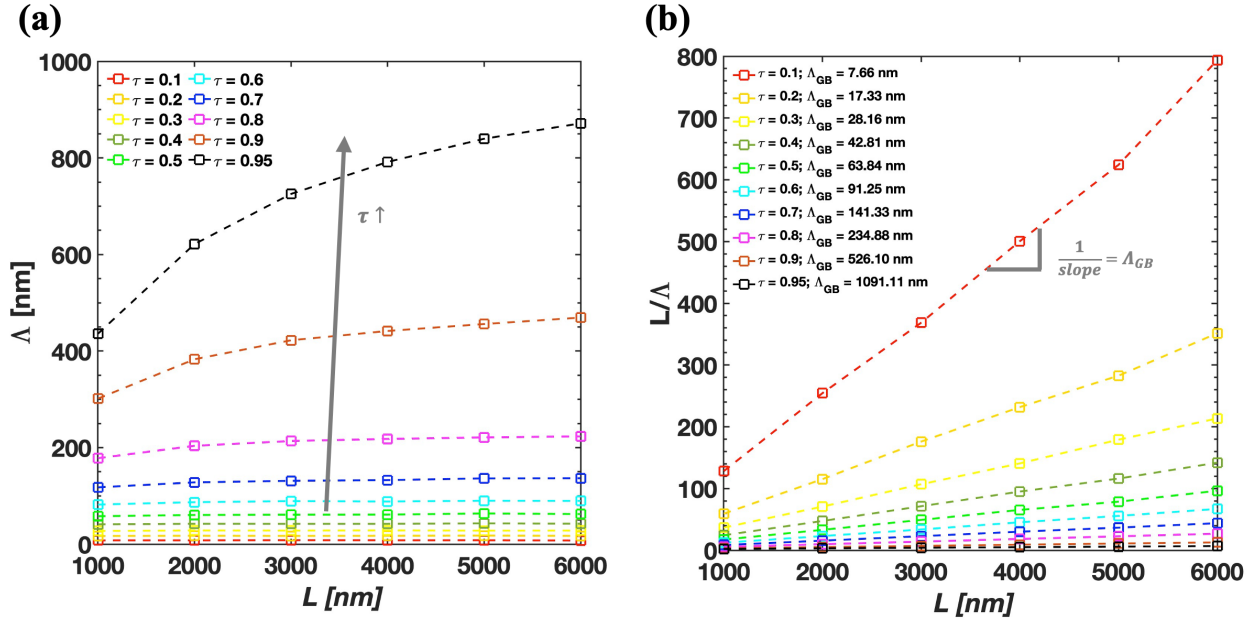
Figure 2.3 | (a) Λ as a function of the simulation length L for different grain boundary transmission probability τ_{GB}. **(b)** Data from a) transformed to obtain the linear relationship between L/Λ and L and calculate the inverse of the slope to obtain Λ_{GB}.

Ray Tracing Robust Fit form:

$$\Lambda_{GB_{Ray\,Trac.}}(\tau_{GB}) = \frac{A_1 \tau_{GB}^{A_2}}{1 - \tau_{GB}}$$

$a_0 = 100nm$
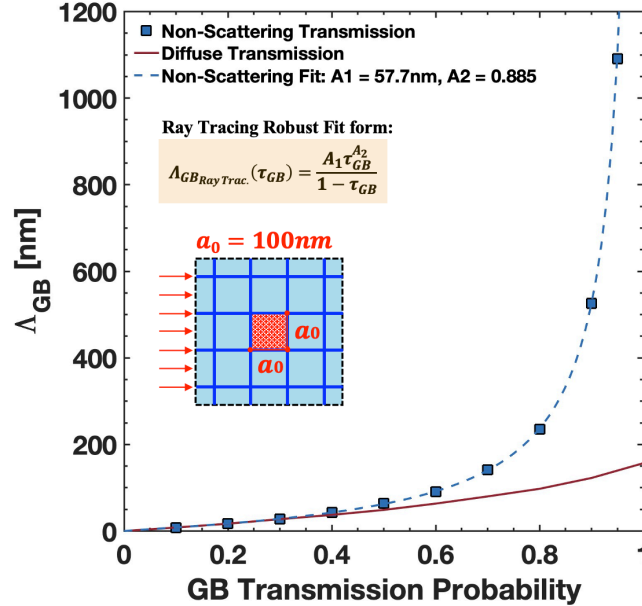
Figure 2.4 | Λ_{GB} as a function of τ_{GB} for the different scattering algorithms.

In our study of phonon-grain boundary scattering, a set of 5 simulations are performed for each τ_{GB} to determine the resulting Λ_{GB} and obtain a nonlinear fitting function, in terms of τ_{GB}, for any given grain structure using equation (7). In each simulation, we launch at least 5×10^5 total phonons to ensure that the fluctuation of $\langle \mathcal{T} \rangle$ is within 5%.

$$\Lambda_{GB}(\tau_{GB}) = \frac{A_1 \tau_{GB}^{A_2}}{1 - \tau_{GB}} \tag{7}$$

where A_1 and A_2 are two fitting parameters depending on the grain size and aspect ratio, respectively. This model function is defined such that the $\Lambda_{GB} \rightarrow \infty$ as $\tau_{GB} \rightarrow 1$, which is consistent with atomistic interpretation between grain boundary transmission probability and phonon mean free path (see **Figure 2.4**).

2.4 Model Validation

Our group has been successfully used ray tracing simulations to compute the boundary scattering mean free path of nanoporous materials with various shapes and distributions [47] as well as nanocomposite materials, with these shapes being inclusion of metallic materials [48]. In this study, we use Monte Carlo ray tracing simulations to capture the phonon mean free path due to grain boundary scattering ($\boldsymbol{\Lambda_{GB}}$) as a function of grain boundary transmission probability, $\boldsymbol{\tau_{GB}(\omega)}$ and then combine a frequency-dependent atomistic expression for grain transmission probability [3], [33] (equation 8) to yield a frequency-dependent mean free path for phonon-grain boundary scattering, $\Lambda_{GB}(\omega)$.

$$\tau_{GB}(\omega) = \frac{1}{\gamma_{RT}\left(\frac{\omega}{\omega_0}\right) + 1} \tag{8}$$

where $\gamma_{RT} = \frac{3}{4} \cdot \frac{1}{\alpha\beta}$ is a generalized fitting parameter that depends on the empirical constant α and the numerical constant β. The former accounts for the effect of grain boundary transmission or the grain boundary quality and material [3]. In the case of silicon materials, a native SiO_2 layer of thickness around 1 nm is usually formed on the outermost surface of each agglomerate if the Si powders are exposed to the atmosphere [49], resulting in oxidized grain boundaries. An oxidized grain boundary yields a smaller α or a larger γ, translating into a lower thermal conductivity. The latter depends on the choice of dispersion relations used in the model and is approximately equals to 0.707 [3]. This frequency-dependent model is qualitatively consistent with atomistic Green's function calculations [50], [51]. The transmissivity approaches one as frequency goes to zero, which is physically consistent with the expectation that long wavelength phonons are unaffected by atomistic disorder at a grain boundary [33]. Combining equation (7) and (8), the resultant $\Lambda_{GB}(\omega)$ is then combined with other mean free paths of phonon scatterings, using Matthiessen's rule under relaxation time approximation, and integrated over a cutoff frequency (ω_0) to obtain the in-plane thermal conductivity. To validate that our modeling can accurately predict the thermal conductivity of nanograined materials, we match the $\Lambda_{GB}(\omega)$ obtained from our ray tracing simulation with the frequency-dependent model proposed by Wang *et al.* in the form of $\Lambda_{GB} = \alpha D_{avg}(\beta\omega_0/\omega)$, where D_{avg} is the average grain size/diameter [3], see **Figure 2.5**. The fitting yields a γ_{RT} of 1.13, and the calculated thermal conductivity is consistent with the experimental data shown on Chapter 3.
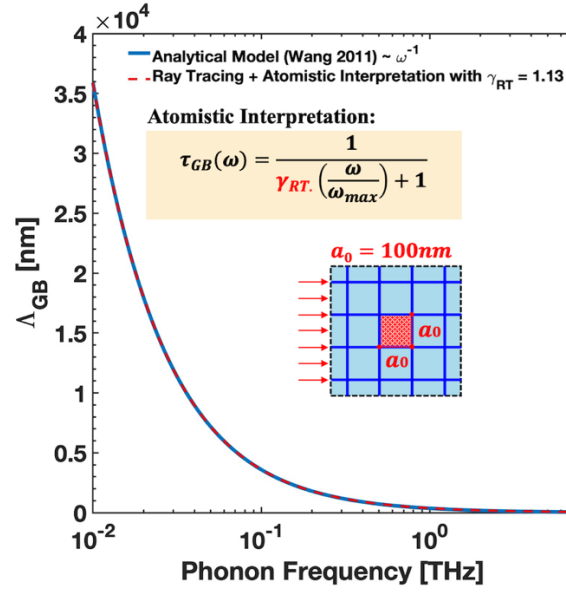
Figure 2.5 | Comparison between the boundary mean free path as a function of phonon frequency given by the analytical formulation (validated with experimental data) and our simulations.

2.5 Lattice Softening Model

To obtain a softened phonon group velocity, we modified the BvK dispersion relation by incorporating a softening factor, F_s, into the isotropic approximation [22] so that the new dispersion relation becomes:

$$\omega = \frac{2}{\pi} F_s v_{bulk} q_0 \sin\left(\frac{\pi q}{2q_0}\right)$$

(9)

where F_s is the ratio of the softened speed of sound to the bulk speed of sound, v_{bulk}, and q is the wavevector. The softened group velocity becomes:

$$v_{g,softend}(\omega) = \frac{\partial \omega}{\partial q} = F_s v_{bulk} \cos\left(\frac{\pi q}{2q_0}\right) = F_s \cdot v_{g,unsoftend}(\omega)$$

(10)

14

For this work, we determine the average softened speed of sound, $v_{s,softened}$, using the following expression [23], [52]:

$$\frac{3}{v_{s,softened}^3} = \frac{1}{v_{long}^3} + \frac{2}{v_{trans}^3} \tag{11}$$

where $v_{long} = \sqrt{E/\rho}$, and $v_{trans} = \sqrt{G/\rho}$ are the longitudinal and transverse speed of sound, respectively; they can be calculated using the elastic and shear moduli obtained from MD simulation for nanograined Si. **Table 1** shows the elastic, shear moduli, softened speed of sounds, and softening factors for nanograined Si with grain areas ranging from 16 nm² to 1024 nm² (i.e. the effective grain sizes ranging from 4nm to 32nm).

2.5 Molecular Dynamics Simulations

The atomistic simulations are performed, using LAMMPS, to study the mechanical behavior of nanograined Si with designed grain heterogeneity and anisotropy. In a 12×12×4 nm³ box, the sample with a squared grain shape is first generated using Voronoi tessellation with randomly assigned grain orientations that ensure the mechanical stability at the corner of the grain, and the effective grain area (on the x-y plane) is 16 nm² for all grains. While fixing the effective grain size and box size, we change the aspect ratio of the horizontal (*x*-axis) and the vertical (*y*-axis) directions to obtain the samples with different grain anisotropy (see Figure 6 and 7). To study the mechanical size effect on the elastic moduli, we then keep the grain heterogeneity of the generated samples unchanged and scale the samples up to 1024 nm² effective grain size, while the total atom number changes from 2.88×10⁴ atoms to 1.47×10⁷ atoms. A Stillinger-Weber potential [53] is applied to describe the interactions of Si atoms. All samples are first equilibrated at 300 K for 50 ps using Nosé-Hoover thermo-stat

[54], [55], then uniaxial tension and shear deformation are performed at a constant engineering strain rate of 5×10^8 s^{-1}. The periodic boundary condition is applied to all three directions (x, y, and z). For 14.7 million atoms, we run 50000 steps under 0.002 ps/timestep for tensile deformation, and the structure is deformed under 5×10 8 s^{-1}, generating 5% strain. As for shear deformation, we run 30000 steps, which generates 3% strain.

CHAPTER 3: RESULTS & DISCUSSION

3.1 Grain Size- and Shape-dependent Elastic Modulus

Large-scale atomistic simulations are performed to study the mechanical behavior of nanograined Si. For the molecular dynamics simulations, three structures with varying grain anisotropy (elongated along the x-direction with an aspect ratio of 2, squared, and elongated along y-direction with an aspect ratio of 1/2) are considered, and each grain in the structures has the same effective grain sizes. With the initial structures, we solely scale the structures to obtain samples with different effective grain sizes and deform the samples under uniaxial tension and shear. **Figure 3.1** shows the corresponding tension strain-stress behaviors for the three structures with different effective grain sizes and their calculated elastic modulus. As shown in **Figure 3.1(d)**, the elastic modulus increases with increasing effective grain size. Interestingly, nanograined Si with an aspect ratio of 2 exhibits the highest elastic modulus in all grain size scales, and nanograined Si with an aspect ratio of 1/2 yields the lowest, suggesting a dependence of the elastic modulus on aspect ratio for grains with the same effective grain size and the deformation anisotropy of nanograined Si. **Figure 3.2** illustrates the shear strain stress behavior and calculated shear modulus for the same three structures. As shown in **Figure 3.2(d)**, the shear modulus also increases with increasing effective grain size, but there is no apparent dependence of shear modulus on the aspect ratio.
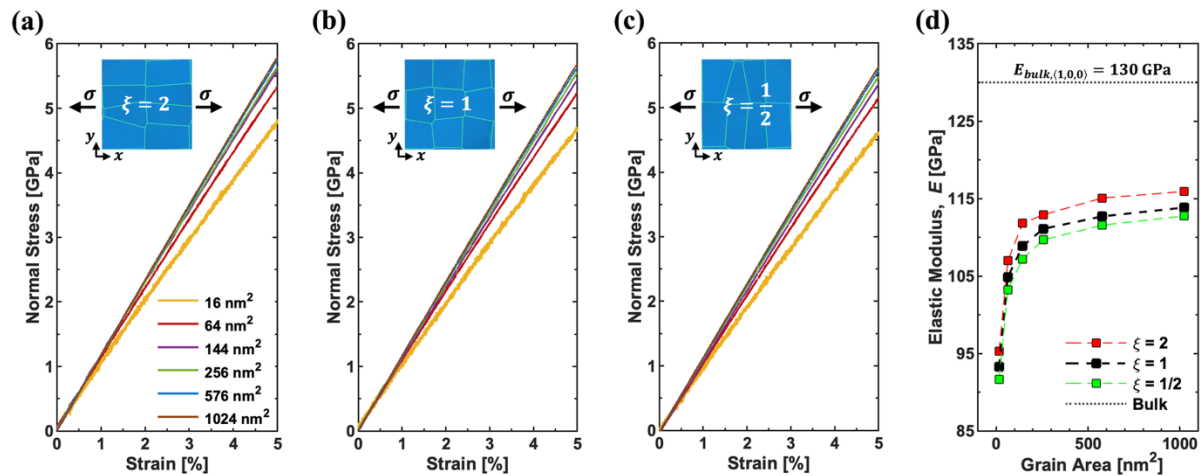
Figure 3.1 | Tension responses of nanograined Silicon. Strain-stress behavior of nanograined silicon with **(a)** $\xi = 2$ (elongated along the x-direction or in-plane direction), **(b)** $\xi = 1$ (square), and **(c)** $\xi = 1/2$ (elongated along the y-direction or cross-plane direction). **(d)** elastic modulus plotted as a function of grain size for the corresponding nanograined structure. The dashed lines denote the reported elastic modulus for bulk nanograined Si in $\langle 1,0,0 \rangle$ direction. The insets demonstrate the grain morphologies, and the black arrows indicate the tension direction.
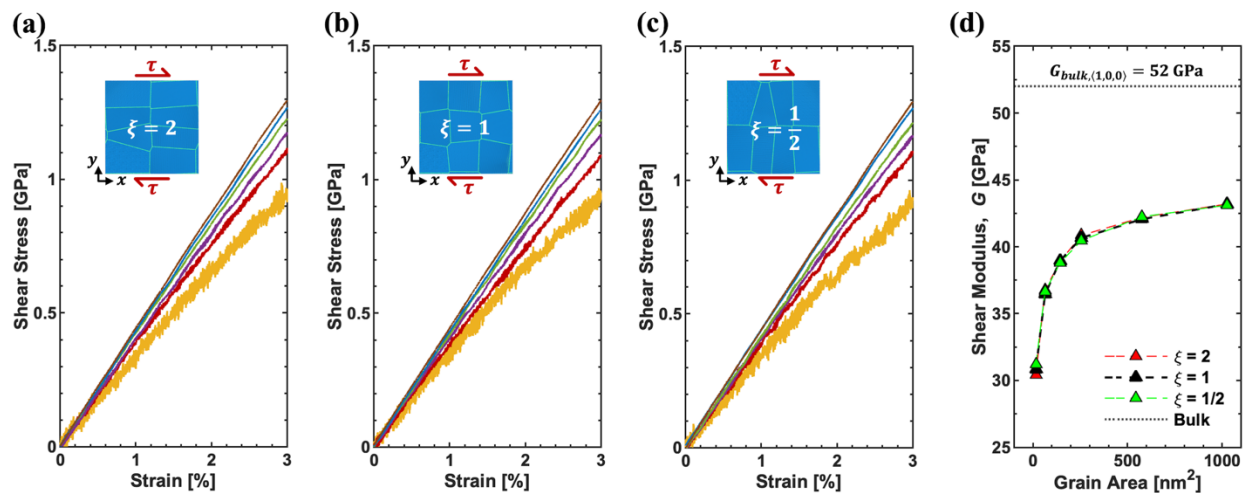
Figure 3.2 | Shear responses of nanograined Silicon. Strain-stress behavior of nanograined silicon with **(a)** $\xi = 2$ (elongated along the x-direction or in-plane direction), **(b)** $\xi = 1$ (square), and **(c)** $\xi = 1/2$ (elongated along the y-direction or cross-plane direction). **(d)** shear modulus plotted as a function of grain size for the corresponding nanograined structure. The dashed lines denote the reported shear modulus for bulk nanograined Si in $\langle 1,0,0 \rangle$ direction. The insets demonstrate the grain morphologies, and the red arrows indicate the shear direction.

Table 1: Elastic, shear moduli, softened speed of sounds, and softening factors for nanograined Si with aspect ratios of $\xi = 1$(square), 2 (elongated along the x-direction), and ½ (elongated along the y-direction). The grain sizes range from 4 nm to 32 nm.

Grain Area (Effective Grain Size)	16 nm² (4 nm)	64 nm² (8 nm)	144 nm² (12 nm)	256 nm² (16 nm)	576 nm² (24 nm)	1024 nm² (32 nm)
Square ($\xi = 1$)						
E (GPa)	93.24	104.87	108.86	111.09	112.69	113.83
G (GPa)	30.83	36.44	38.96	40.66	42.06	43.17
$v_{s,softened}$ [m/s]	4042	4384	4527	4619	4694	4751
F_s	0.664	0.721	0.744	0.759	0.772	0.781
Elongated along the x – direction ($\xi = 2$)						
E (GPa)	95.27	106.96	111.81	112.89	115.05	115.91
G (GPa)	30.42	36.74	38.92	40.85	42.19	43.19
$v_{s,softened}$ [m/s]	4021	4404	4531	4633	4705	4757
F_s	0.661	0.724	0.745	0.762	0.773	0.782
Elongated along the y – direction ($\xi = 1/2$)						
E (GPa)	91.63	103.22	107.19	109.66	111.56	112.74
G (GPa)	31.20	36.63	38.81	40.46	42.24	43.10
$v_{s,softened}$ [m/s]	4060	4391	4516	4606	4700	4745
F_s	0.667	0.722	0.742	0.757	0.773	0.780
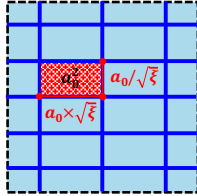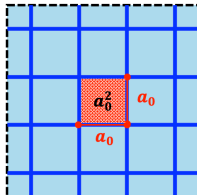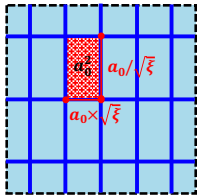
While decreasing the effective grain size to the nano regime, the grain boundary density will increase rapidly, which enhances the significant role of grain boundary in mechanical deformation. Unlike the grain interior, where atoms follow regular packing patterns, grain boundary atoms tend to have random arrangements. This reduces the interatomic bonding between grain boundary atoms and makes them ultimately weaker than regularly packed atoms. When nanograined Si is under tension, in the elastic regime, the atoms are purely stretched along the loading direction. With the introduction of grain anisotropy defined by the grain aspect ratio, the portion of grain boundary atoms along the loading direction changes. This influences the stretchability of the grain structure during tension, and thus the elastic modulus. In other words, the more grain boundary atoms are

along the loading direction, the softer the nanograined Si will be. Nevertheless, the fact that the elongation direction does not perfectly align with the shear direction diminishes the contribution of grain anisotropy to the shear deformation.

3.2 Effect of Grain Anisotropy on Grain Boundary Scattering Mean Free Path

Extreme grain elongations or large grain aspect ratios could result from using nanowires as precursors to pallets in which the alignment can potentially be achieved using techniques like flow [56] and magnetic alignments [57] or nanowire combing [58]. To investigate the effect of grain anisotropy on phonon-grain boundary scattering mean free path, thermal conductivity, and thermal anisotropy, we construct anisotropic grain structures with a fixed grain area of $(100nm)^2$ or constant grain boundary density and vary their grain aspect ratios ξ from 1/256 to 256 in powers of 2 increments. As demonstrated in Chapter 2, we first use MCRT simulations to capture the phonon-grain boundary scattering mean free path $\mathbf{\Lambda}_{GB}(\tau_{GB})$ as a function of grain boundary transmission probability, and then convert it into a frequency-dependent mean free path $\mathbf{\Lambda}_{GB}(\omega)$ by applying an atomistic relationship between transmission probability and phonon frequency $\boldsymbol{\tau}_{GB}(\boldsymbol{\omega})$. **Table 2** shows the grain boundary mean free path fitting parameters from ray tracing simulations and the interfacial densities for corresponding grain structures. The interfacial density is defined as the perimeter of the grain divided by the area of the grain, $\phi = 2 \times [(a_0 \times \sqrt{\xi}) + (a_0/\sqrt{\xi})]/a_0^2$, and the interfacial density along the heat flux direction is defined as one over the horizontal grain size, $\phi_x = 1/(a_0 \times \sqrt{\xi})$.

Table 2: Grain boundary MFP Fitting Parameters and Interfacial Density

ξ	A_1 [nm]	A_2	ϕ [μm⁻¹]	ϕ_x [μm⁻¹]	Configurations*
■ 256	48.3	0.388	321.3	0.63	
■ 128	56.7	0.386	228.0	0.88	
■ 64	63.4	0.382	162.5	1.25	
■ 32	69.5	0.357	116.7	1.77	
■ 16	74.7	0.442	85.0	2.50	
■ 8	78.2	0.552	63.6	3.54	
■ 4	79.7	0.781	50.0	5.00	
■ 2	70.1	0.850	42.4	7.07	
■ 1	57.7	0.885	40.0	10.0	
■ 1/2	45.8	0.932	42.4	14.1	
■ 1/4	34.7	0.978	50.0	20.0	
■ 1/8	25.1	0.962	63.6	28.3	
■ 1/16	18.2	0.988	85.0	40.0	
■ 1/32	13.1	0.981	116.7	56.6	
■ 1/64	9.34	0.992	162.5	80.0	
■ 1/128	6.59	0.995	228.0	113.1	
■ 1/256	4.80	1.03	321.3	160.0	

*The insets show the simulated unit cells with varying grain heterogeneity characterized by an aspect ratio, ξ. (e.g. $\xi = 1$ represents a square grain geometry; $\xi > 1$ yields a rectangular grain geometry elongates along the x-direction, and vice versa for the y-direction). a_0 denotes the effective grain size, and the aspect ratio is defined such that the grain area a_0^2 remains unchanged. The interfacial density is defined as the perimeter of the grain divided by the area of the grain, $\phi = 2 \times [(a_0 \times \sqrt{\xi}) + (a_0/\sqrt{\xi})]/a_0^2$, and the interfacial density along the heat flux direction is defined as one over the horizontal grain size, $\phi_x = 1/(a_0 \times \sqrt{\xi})$.

(a)

Grain Area: $(100\ nm)^2$

$a_0/\sqrt{\xi}$

$\xi\uparrow$

$a_0\times\sqrt{\xi}$

Ray Tracing Robust-Fit Form:

$$\Lambda_{GB_{RayTrac.}}(\tau_{GB}) = \frac{A_1 \tau_{GB}^{A_2}}{1-\tau_{GB}}$$

Λ_{GB} [nm]

Grain Boundary Transmission Probability, τ_{GB}

(b)

Atomistic Interpretation:

$$\tau_{GB}(\omega) = \frac{1}{\gamma_{RT}\left(\frac{\omega}{\omega_0}\right)+1}$$

Λ_{GB} [nm]

Phonon Frequency [THz]

(c)

$\left\langle\frac{1}{\Lambda_{eff}}\right\rangle$

$\left\langle\frac{1}{\Lambda_{imp.}}\right\rangle$ $\left\langle\frac{1}{\Lambda_{umkl.}}\right\rangle$ $\left\langle\frac{1}{\Lambda_{GB}}\right\rangle$

Accumulated Inverse MFP, $\langle 1/\Lambda\rangle$ [nm^{-1}]

Accumulated Inverse MFP: $\left\langle\frac{1}{\Lambda_i}\right\rangle = \int_0^{\omega_0} \frac{1}{\Lambda_i(\omega)}d\omega$

Matthiessen's Rule:

$$\left\langle\frac{1}{\Lambda_{eff}}\right\rangle = \left\langle\frac{1}{\Lambda_{umkl.}}\right\rangle + \left\langle\frac{1}{\Lambda_{imp.}}\right\rangle + \left\langle\frac{1}{\Lambda_{GB}}\right\rangle$$

Temperature [K]

.... Impurity
– – – Umklapp   ▬▬ $\xi = 1$
——— $\xi = 256$ ——— $\xi = 1/256$
——— $\xi = 128$ ——— $\xi = 1/128$
——— $\xi = 64$ ——— $\xi = 1/64$
——— $\xi = 32$ ——— $\xi = 1/32$
——— $\xi = 16$ ——— $\xi = 1/16$
——— $\xi = 8$ ——— $\xi = 1/8$
——— $\xi = 4$ ——— $\xi = 1/4$
——— $\xi = 2$ ——— $\xi = 1/2$
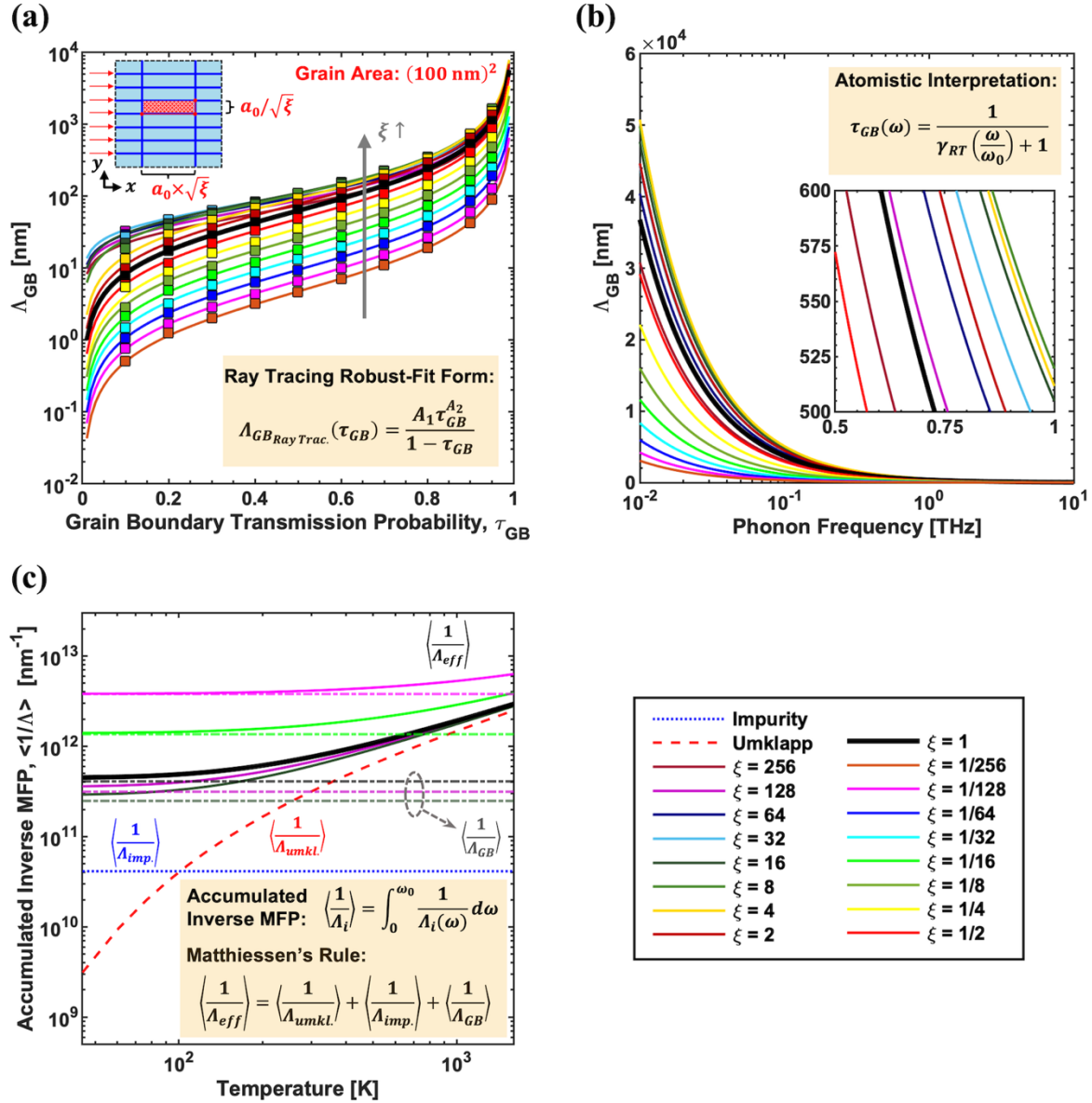
Figure 3.3 | Phonon mean free paths of nanograined silicon with a constant grain area of $10000\ nm^2$. (a) Resulting phonon-boundary scattering mean free path Λ_{GB} as a function of grain boundary transmission probability and **(b)** phonon frequency. Λ_{GB} monotonically increases with increasing transmission probability and decreases with phonon frequency. The simulation results show various grain aspect ratios ranging from 1/256 to 256 with an increment of two. **(c)** Inverse of effective mean free paths of nanograined silicon as a function of temperature. The mean free paths for phonon-boundary scattering and impurity scattering are independent of temperature, whereas the mean free paths for Umklapp scattering increases with increasing temperature. This plot illustrates the weight of each scattering contribution across a temperature range from 10 to 1250K.

Figure 3.3(a) and **(b)** show the resulting grain boundary scattering mean free path as a function of grain boundary transmission probability and phonon frequency, respectively. Λ_{GB} monotonically increases with increasing transmission probability and decreases with increasing phonon frequency. This behavior is quantitively consistent with the fact that long wavelength phonons (low frequency) are unaffected by atomistic disorder at a grain boundary [33]. We notice that Λ_{GB} generally increases with increasing aspect ratio; however, the curves start to flatten for $\xi \geq 16$, resulting in an inverse trend at high grain boundary transmission probabilities (e.g. $\tau > 0.3$) for these grain boundary structures. This trend can be explained by the fitting parameters of Eq. (7), which manifest the flattening of the curves for high aspect ratios with a decreasing A_2. The Λ_{GB} is largest over a wide range of phonon frequencies when the aspect ratio is about 16 (see **Figure 3.3(b)**). **Figure 3.3(c)** shows the accumulated inverse mean free paths as a function of temperature. The accumulated inverse mean free path is calculated by integrating $1/\Lambda_i(\omega)$ over the frequencies range from 0 to the cut-off frequency, ω_0, where i denotes the type of scattering mechanism. In this way, we can better visualize the contribution of each scattering mechanism over the temperature range without being affected by its frequency-dependency. As shown on **Figure 3.3(c)**, the contribution from impurity scattering and grain boundary scattering remains constant while that from Umklapp scattering increases with increasing temperature. The solid lines show the inverse of average effective mean free path given by the Matthiessen's rule. Clearly, the effective mean free path of nanograined silicon is dominated by grain boundary scattering at the low temperature limit ($T \ll \theta_D$) and Umklapp scattering at the high temperature limit ($T \gg \theta_D$). This is consistent with the classical model

that the mean free path of silicon decreases with an increase in temperature, leading to a reduction in thermal conductivity at the high temperature limit.

3.3 Effect of Grain Heterogeneity on Thermal Anisotropy

Figure 3.4 shows the temperature-dependent thermal conductivity of nanograined Si for the same grain area of 10000 nm² but with different grain aspect ratios. The thermal conductivity first increases with increasing temperature, reaches a maximum value at some intermediate temperature, and then decreases with elevated temperature due to substantial Umklapp scattering at the high temperature limit ($T \gg \theta_D$). For $\xi < 1$, the thermal conductivity decreases with decreasing aspect ratios. This can be justified by the increase in interfacial density in the direction of heat flux Φ_x (i.e., an increase in the number of vertical grain boundary lines) – see **Table 2**. These vatical grain boundaries serve as obstacles that reflect and impede the movement of phonons, resulting in a shorter phonon mean free path. For $\xi > 1$, there is an optimal ξ that maximizes the thermal conductivity, and a grain structure with an aspect ratio of 16 yields the highest thermal conductivity at a temperature of around 150K. For $\xi > 16$, the thermal conductivity starts to decrease with increasing aspect ratio. This can be attributed to the substantial scattering of low-frequency phonon with anisotropic grain boundaries. In other words, the spacing between horizontal grain boundaries collapse for larger aspect ratio, which limits the transport of long wavelength (low frequency) phonons.
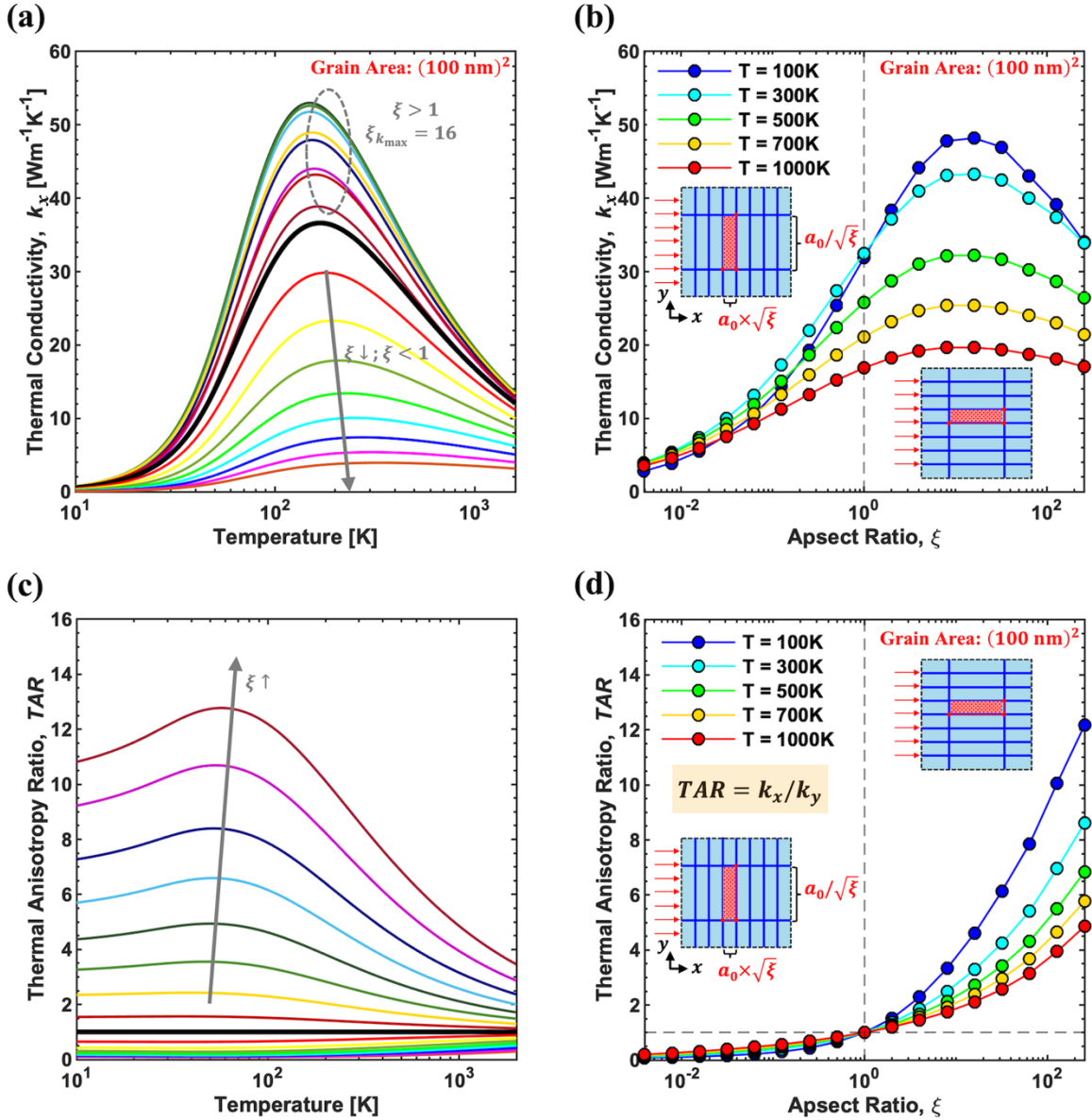
Figure 3.4 | (a) Temperature-dependent thermal conductivity of nanograined Si for different grain aspect ratios. **(b)** Thermal conductivity of nanograined Si as a function of grain aspect ratio. **(c)** Thermal anisotropy ratio of nanograined Si as a function of temperature, and **(d)** grain aspect ratios, respectively. The results share the same grain structures from the previous section and are computed by integrating the BTE with the resulting effective mean free path and BvK dispersion relationship over the maximum phonon frequency for Si.

It's worth restating that the thermal conductivity presented in the above figure corresponds to the directional thermal conductivity in the direction of heat flux, also known

as the in-plane thermal conductivity (k_x). Since we have two sets of grain structures with aspect ratios $\xi > 1$ and $\xi < 1$ at the same increment of two, a grain geometry with $\xi = 1/2$ is a counterpart that rotates 90° from a grain geometry with $\xi = 2$. Namely, the in-plane thermal conductivity for a grain geometry with $\xi = 1/2$ is therefore the cross-plane thermal conductivity, k_y, for a grain geometry with $\xi = 2$. As a result, we define the thermal anisotropy ratio as k_x/k_y. As shown in **Figure 3.4(d)**, the thermal anisotropy ratio monotonically increases with grain aspect ratios up to 256 even at high temperatures; however, the increase in thermal anisotropy ratio from an increasing aspect ratio is less prominent at higher temperature because the thermal transport is dominant by Umklapp scattering at the high temperature limit.

3.4 Phonon Softening Effect in Nanograined Silicon
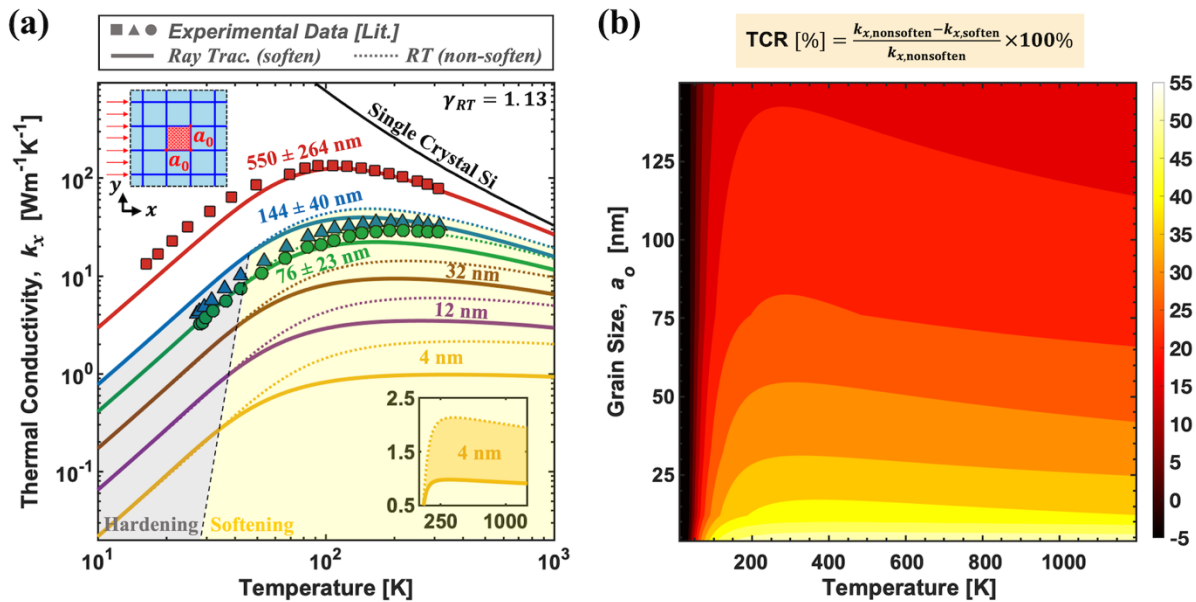
Figure 3.5 | (a) Temperature-dependent thermal conductivity of nanograined Si for a grain aspect ratio of 1 (square geometry) with different grain sizes a_0. The dash lines show the thermal conductivity using the BvK dispersion for bulk silicon (without accounting for the change in phonon group velocity due to lattice softening). The solid lines show the size-dependent thermal conductivity accounting for the lattice softening effect. The correction is

made using a modified BvK dispersion relation along with a softening factor governed by mechanical properties from the MD simulation. The scatter points are experiential data from Wang, et al.[3] **(b)** Contour plot showing the thermal conductivity reduction (%) as a function of both the temperature and effective grain sizes.

**Figure 3.5(a)** shows the thermal conductivity of square nanograined Si as a function of temperature. The scatter points are experiential data from Wang, *et al* [3]. The dash lines show the thermal conductivity of nanograined silicon without accounting for the lattice softening effect, and the solid lines show the corrected thermal conductivity using the modified BvK dispersion relation. In general, the lattice softening effect is more prominent for nanograined Si with smaller grain size and at high temperature. As the grain size increases, we observe that the solid line slowly converges to the dash lines. This is because the mechanical properties of nanograined silicon slowly converge to the bulk limit for some large grain sizes that the softening effect becomes negligible. Using the extrapolated prediction from the MD mechanical properties, we found this limit to be somewhere around 125 to 140nm (see **Figure 3.6**). Hence, for nanograined silicon with a grain size larger than 140nm, it's reasonable to assume a softening factor of 1 (i.e., using the conventional bulk group velocity for the thermal conductivity calculation). It's worth mentioning that the effective grain size from the previous section (100nm) is below this limit, and therefore the thermal conductivity is affected by the lattice softening effect; however, we assume the softening effect be negligible to better observe the effect of grain anisotropy on the thermal properties.
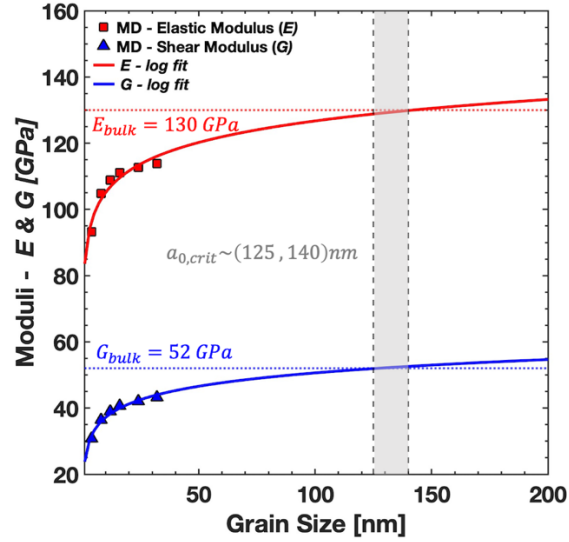
Figure 3.6 | Logarithmic fit of the moduli of square nanograined silicon as a function of grain size. As the grain size increases, the elastic modulus and shear modulus converge to the bulk values for some grain sizes between 125 and 140 nm. This implies that the lattice softening effect becomes negligible for nanograined silicon with a grain size larger than 140 nm. For any grain size smaller than 140 nm (lattice softening regimes), we need to apply the softening factor for the thermal conductivity correction.

With decreasing grain size and increasing temperature, the reduction in thermal conductivity becomes more significant. A nanograined silicon with an average grain size of 4 nm shows about 50% reduction in thermal conductivity at a temperature greater than 200K. While the lattice softening effect reduces high temperature thermal conductivity, it increases the low-temperature thermal conductivity. As shown on **Figure 3.5(b)**, this increase is less than 5% for nanograined silicon at the low temperature limit ($T \ll \theta_D$). Indeed, this "hardening" effect at the low temperature limit can be attributed to the competing effect between the increase in volumetric specific heat capacity and the decrease in effective phonon mean free path due to a lower group velocity. In order to justify this phenomenon observed from the modeling. We need to look at the dependence of group velocity on the volumetric specific heat capacity and the effective mean free path,

respectively, at the different temperature limits. We know that $\Lambda_{eff} = v_g \tau_{eff} \propto v_g^1$; hence, reducing the group velocity while keeping the bulk volumetric specific heat capacity would result in a thermal conductivity reduction across the whole temperature range (as indicated by the green curve on **Figure 3.7**). However, the volumetric specific heat capacity has different behaviors at the low-temperature limit ($T \ll \theta_D$) and the high temperature limit ($T \gg \theta_D$). The volumetric specific heat capacity, $C_v = \frac{12\pi^4}{5} n_a k_B \left(\frac{T^3}{\theta_D^3}\right) \propto \frac{1}{\theta_D^3} \propto v_g^{-3}$, is proportional to v_g^{-3} at the low-temperature limit and is independent of the change in group velocity at the high-temperature limit (i.e. $C_v \propto v_g^0$). Therefore, reducing the group velocity while keeping the bulk mean free path would result in a significantly increase in the thermal conductivity from low to intermediate temperatures (as indicated by the red curve on **Figure 3.7**). As a result, the "hardening" effect occurs when the contribution of softened group velocity on the volumetric specific heat capacity is higher than that on the mean free path.
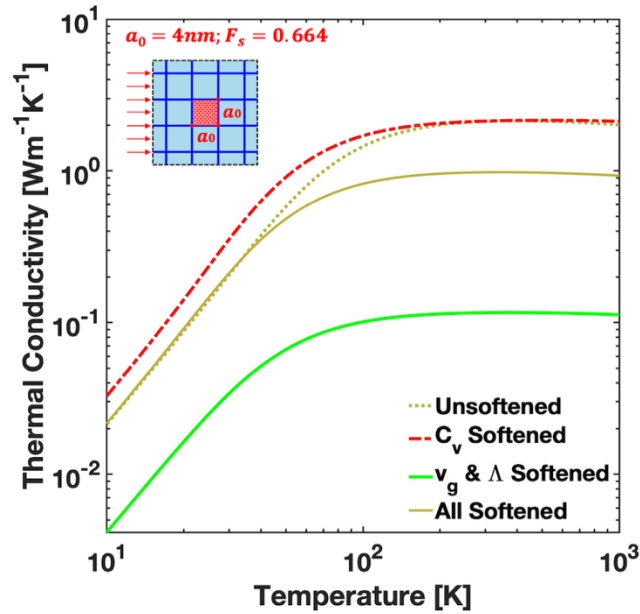
Figure 3.7 | Contributions of softened group velocity on the volumetric specific heat capacity and mean free path, respectively.

CHAPTER 4: SUMMARY AND CONCLUSIONS

This thesis work leads to two major conclusions. First, we demonstrate that it is possible to achieve thermomechanical anisotropy in nanograined silicon by tailoring the aspect ratio of the nanograin structure. To this end, we establish a simulation framework using heat-flux driven Monte Carlo ray tracing simulations, which we validate by comparing the frequency-dependent treatments at the grain boundaries to experimental data. Our ray tracing simulation results show that reducing the material grain size (i.e., increasing grain boundary density) effectively decreases the thermal conductivity due to the dense network of grain boundary interfaces that scatter phonons. Furthermore, our results for ideal grain structures reveal that a flexible degree of thermal anisotropy can be achieved within different aspect ratios, which could be obtained by using nanowires as precursors for bulk materials. We also find that the elastic modulus at the nanoscale is highly dependent on the grain size, where the grain boundaries are held responsible.

Second, the lattice softening effect reduces high-temperature thermal conductivity and increases the low-temperature thermal conductivity of nanograined silicon. While the mechanical properties of nanograined silicon decrease with reducing grain size, the high-temperature thermal conductivity decreases significantly due to lattice softening. To account for the lattice softening effect on the thermal conductivity, we use the elastic moduli and shear moduli obtained from MD simulation and establish their relationship with the speed of sound to modify the exiting BvK dispersion relation for bulk silicon and hence the phonon group velocity. The modeling results suggest that the lattice softening effect is more prominent for smaller grain sizes at the high-temperature limit.

In summary, controlling the grain size and aspect ratio of a nanostructure is crucial for achieving optimal thermal conductivity reduction and thermal anisotropy. Our presented guidelines for reducing the thermal conductivity using grain boundary scattering and lattice softening and introducing thermal anisotropy in nanocrystalline materials highlights the microstructure-engineering of tunable thermomechanical property and have meaningful impact on multifunctional materials for applications in thermoelectric cooling, power generation, and heat-guiding structures.

REFERENCES

[1]   A. I. Boukai, Y. Bunimovich, J. Tahir-Kheli, J. K. Yu, W. A. Goddard, and J. R. Heath, "Silicon nanowires as efficient thermoelectric materials," *Nature*, vol. 451, no. 7175, pp. 168–171, 2008, doi: 10.1038/nature06458.

[2]   A. I. Hochbaum *et al.*, "Enhanced thermoelectric performance of rough silicon nanowires," *Nature*, vol. 451, no. 7175, pp. 163–167, Jan. 2008, doi: 10.1038/nature06381.

[3]   Z. Wang, J. E. Alaniz, W. Jang, J. E. Garay, and C. Dames, "Thermal conductivity of nanocrystalline silicon: Importance of grain size and frequency-dependent mean free paths," *Nano Lett*, vol. 11, no. 6, pp. 2206–2213, Jun. 2011, doi: 10.1021/nl1045395.

[4]   T. Hori, J. Shiomi, and C. Dames, "Effective phonon mean free path in polycrystalline nanostructures," *Appl Phys Lett*, vol. 106, no. 17, Apr. 2015, doi: 10.1063/1.4918703.

[5]   S. Alaie, D. F. Goettler, M. Su, Z. C. Leseman, C. M. Reinke, and I. El-Kady, "Thermal transport in phononic crystals and the observation of coherent phonon scattering at room temperature," *Nat Commun*, vol. 6, Jun. 2015, doi: 10.1038/ncomms8228.

[6]   P. E. Hopkins *et al.*, "Reduction in the thermal conductivity of single crystalline silicon by phononic crystal patterning," *Nano Lett*, vol. 11, no. 1, pp. 107–112, Jan. 2011, doi: 10.1021/nl102918q.

[7]   J. Lee, J. Lim, and P. Yang, "Ballistic phonon transport in holey silicon," *Nano Lett*, vol. 15, no. 5, pp. 3273–3279, May 2015, doi: 10.1021/acs.nanolett.5b00495.

[8]   W. Park *et al.*, "Impact of thermally dead volume on phonon conduction along silicon nanoladders," *Nanoscale*, vol. 10, no. 23, pp. 11117–11122, Jun. 2018, doi: 10.1039/c8nr01788c.

[9]   D. Li, Y. Wu, P. Kim, L. Shi, P. Yang, and A. Majumdar, "Thermal conductivity of individual silicon nanowires," *Appl Phys Lett*, vol. 83, no. 14, pp. 2934–2936, Oct. 2003, doi: 10.1063/1.1616981.

[10]   J. K. Yu, S. Mitrovic, D. Tham, J. Varghese, and J. R. Heath, "Reduction of thermal conductivity in phononic nanomesh structures," *Nat Nanotechnol*, vol. 5, no. 10, pp. 718–721, 2010, doi: 10.1038/nnano.2010.149.

[11]   J. Lee *et al.*, "Investigation of phonon coherence and backscattering using silicon nanomeshes," *Nat Commun*, vol. 8, Jan. 2017, doi: 10.1038/ncomms14054.

[12]   L. Yang, Y. Zhao, Q. Zhang, J. Yang, and D. Li, "Thermal transport through fishbone silicon nanoribbons: Unraveling the role of Sharvin resistance," *Nanoscale*, vol. 11, no. 17, pp. 8196–8203, May 2019, doi: 10.1039/c9nr01855g.

[13] K. Li *et al.*, "The Deformation and Ageing of Mild Steel: III Discussion of Results You may also like Research of thermal oxygen ageing on tensile properties of rubber based on Peck-Yeoh model On the influence of morphology and chemical defects on charge transport dynamics in polyethylene: thermal ageing and concentration gradient Influence of Cycling Profile, Depth of Discharge and Temperature on Commercial LFP/C Cell Ageing: Cell Level Analysis with ICA, DVA and OCV Measurements."

[14] C. v. di Leo and J. J. Rimoli, "New perspectives on the grain-size dependent yield strength of polycrystalline metals," *Scr Mater*, vol. 166, pp. 149–153, Jun. 2019, doi: 10.1016/j.scriptamat.2019.03.019.

[15] N. Tsuji, Y. Ito, Y. Saito, and Y. Minamino, "Strength and ductility of ultrafine grained aluminum and iron produced by ARB and annealing." [Online]. Available: www.actamat-journals.com

[16] J. Schiøtz, F. D. di Tolla, and K. W. Jacobsen, "Softening of nanocrystalline metals at very small grain sizes," *Nature*, vol. 391, no. 6667, pp. 561–563, Feb. 1998, doi: 10.1038/35328.

[17] N. Hansen, "Hall-petch relation and boundary strengthening," *Scr Mater*, vol. 51, no. 8 SPEC. ISS., pp. 801–806, 2004, doi: 10.1016/j.scriptamat.2004.06.002.

[18] O. A. Ageev, E. Y. Gusev, J. Y. Jityaeva, M. v. Ilina, and A. v. Bykov, "Grain size and doping effect on structure and electromechanical properties of polycrystalline silicon for MEMS applications," in *Journal of Physics: Conference Series*, Institute of Physics Publishing, Sep. 2016. doi: 10.1088/1742-6596/741/1/012001.

[19] V. I. Ivashchenko, P. E. A. Turchi, and V. I. Shevchenko, "Simulations of the mechanical properties of crystalline, nanocrystalline, and amorphous SiC and Si," *Phys Rev B Condens Matter Mater Phys*, vol. 75, no. 8, Feb. 2007, doi: 10.1103/PhysRevB.75.085209.

[20] W. N. Sharpe, K. T. Turner, and R. L. Edwards, "Tensile Testing of Polysilicon." [Online]. Available: http://mems.mcnc.org/mumps.html

[21] S. Goel, A. Kovalchenko, A. Stukowski, and G. Cross, "Influence of microstructure on the cutting behaviour of silicon," *Acta Mater*, vol. 105, pp. 464–478, Feb. 2016, doi: 10.1016/j.actamat.2015.11.046.

[22] M. D. Gerboth and D. G. Walker, "Effects of acoustic softening on thermal conductivity beyond group velocity," *J Appl Phys*, vol. 127, no. 20, p. 204302, May 2020, doi: 10.1063/1.5135584.

[23] R. Hanus *et al.*, "Lattice Softening Significantly Reduces Thermal Conductivity and Leads to High Thermoelectric Efficiency," *Advanced Materials*, vol. 31, no. 21, May 2019, doi: 10.1002/adma.201900108.

[24] J. F. Li, W. S. Liu, L. D. Zhao, and M. Zhou, "High-performance nanostructured thermoelectric materials," *NPG Asia Materials*, vol. 2, no. 4. pp. 152–158, Oct. 2010. doi: 10.1038/asiamat.2010.138.

[25] M. A. Hopcroft, W. D. Nix, and T. W. Kenny, "What is the Young's modulus of silicon?," *Journal of Microelectromechanical Systems*, vol. 19, no. 2, pp. 229–238, Apr. 2010, doi: 10.1109/JMEMS.2009.2039697.

[26] M. S. Jeng, R. Yang, D. Song, and G. Chen, "Modeling the thermal conductivity and phonon transport in nanoparticle composites using Monte Carlo simulation," in *Journal of Heat Transfer*, American Society of Mechanical Engineers(ASME), 2008. doi: 10.1115/1.2818765.

[27] S. Mazumder and A. Majumdar, "Monte Carlo study of phonon transport in solid thin films including dispersion and polarization," *J Heat Transfer*, vol. 123, no. 4, pp. 749–759, Aug. 2001, doi: 10.1115/1.1377018.

[28] D. Lacroix, K. Joulain, and D. Lemonnier, "Monte Carlo transient phonon transport in silicon and germanium at nanoscales," *Phys Rev B Condens Matter Mater Phys*, vol. 72, no. 6, Aug. 2005, doi: 10.1103/PhysRevB.72.064305.

[29] J. Ma *et al.*, "Coherent phonon-grain boundary scattering in silicon inverse opals," *Nano Lett*, vol. 13, no. 2, pp. 618–624, Feb. 2013, doi: 10.1021/nl304190s.

[30] C. Kimmer, S. Aubry, A. Skye, and P. K. Schelling, "Scattering of phonons from a high-energy grain boundary in silicon: Dependence on angle of incidence," *Phys Rev B Condens Matter Mater Phys*, vol. 75, no. 14, Apr. 2007, doi: 10.1103/PhysRevB.75.144105.

[31] C. Hua, X. Chen, N. K. Ravichandran, and A. J. Minnich, "Experimental metrology to obtain thermal phonon transmission coefficients at solid interfaces," *Phys Rev B*, vol. 95, no. 20, May 2017, doi: 10.1103/PhysRevB.95.205423.

[32] Q. Hao *et al.*, "Theoretical studies on the thermoelectric figure of merit of nanograined bulk silicon," *Appl Phys Lett*, vol. 97, no. 6, Aug. 2010, doi: 10.1063/1.3478459.

[33] C. Hua and A. J. Minnich, "Importance of frequency-dependent grain boundary scattering in nanocrystalline silicon and silicon-germanium thermoelectrics," *Semicond Sci Technol*, vol. 29, no. 12, Dec. 2014, doi: 10.1088/0268-1242/29/12/124004.

[34] D. Chakraborty, S. Foster, and N. Neophytou, "Monte Carlo phonon transport simulations in hierarchically disordered silicon nanostructures," *Phys Rev B*, vol. 98, no. 11, Sep. 2018, doi: 10.1103/PhysRevB.98.115435.

[35] L. Yang and A. J. Minnich, "Thermal transport in nanocrystalline Si and SiGe by ab initio based Monte Carlo simulation," *Sci Rep*, vol. 7, Mar. 2017, doi: 10.1038/srep44254.

[36] H. Yang *et al.*, "Enhanced thermoelectric properties in bulk nanowire heterostructure-based nanocomposites through minority carrier blocking," *Nano Lett*, vol. 15, no. 2, pp. 1349–1355, Feb. 2015, doi: 10.1021/nl504624r.

[37] H. Fang and Y. Wu, "Telluride nanowire and nanowire heterostructure-based thermoelectric energy harvesting," *J Mater Chem A Mater*, vol. 2, no. 17, pp. 6004–6014, May 2014, doi: 10.1039/c3ta14129b.

[38] C. Kittel, *Introduction to Solid State Physics*, 8th ed. NJ: Wiley: Hoboken, 2004.

[39] T. P. R. C. (TPRC). Purdue University, Ed., *Thermophysical Properties of Matter*, Touloukian, Y. S. New York: IFI/Plenum, 1970.

[40] F. Yang and C. Dames, "Mean free path spectra as a tool to understand thermal conductivity in bulk and nanostructures," *Phys Rev B Condens Matter Mater Phys*, vol. 87, no. 3, Jan. 2013, doi: 10.1103/PhysRevB.87.035437.

[41] P. G. Klemens -~, "Phonon Scattering and Thermal Resistance Due to Grain Boundaries ~," 1994.

[42] Y. Ikoma, K. Matsuda, K. Yoshida, M. Takaira, and M. Kohno, "Electric, thermal, and optical properties of severely deformed Si processed by high-pressure torsion," *J Appl Phys*, vol. 132, no. 21, Dec. 2022, doi: 10.1063/5.0122826.

[43] L. Chen, J. L. Braun, B. F. Donovan, P. E. Hopkins, and S. J. Poon, "Ballistic transport of long wavelength phonons and thermal conductivity accumulation in nanograined silicon-germanium alloys," *Appl Phys Lett*, vol. 111, no. 13, Sep. 2017, doi: 10.1063/1.4986884.

[44] C. Jeong, S. Datta, and M. Lundstrom, "Full dispersion versus Debye model evaluation of lattice thermal conductivity with a Landauer approach," in *Journal of Applied Physics*, Apr. 2011. doi: 10.1063/1.3567111.

[45] S. Datta, *Electronic Transport in Mesoscopic Systems*. Cambridge University Press, 1995. doi: 10.1017/CBO9780511805776.

[46] J. S. Heron, C. Bera, T. Fournier, N. Mingo, and O. Bourgeois, "Blocking phonons via nanoscale geometrical design," *Phys Rev B Condens Matter Mater Phys*, vol. 82, no. 15, Oct. 2010, doi: 10.1103/PhysRevB.82.155458.

[47] Z. Yu, L. Ferrer-Argemi, and J. Lee, "Investigation of thermal conduction in symmetric and asymmetric nanoporous structures," *J Appl Phys*, vol. 122, no. 24, Dec. 2017, doi: 10.1063/1.5006818.

[48] L. Ferrer-Argemi, Z. Yu, and J. Lee, "Effects of metal silicide inclusion interface and shape on thermal transport in silicon nanocomposites," *J Appl Phys*, vol. 126, no. 3, Jul. 2019, doi: 10.1063/1.5099507.

[49] M. Morita, T. Ohmi, E. Hasegawa, M. Kawakami, and M. Ohwada, "Growth of native oxide on a silicon surface," *J Appl Phys*, vol. 68, no. 3, pp. 1272–1281, 1990, doi: 10.1063/1.347181.

[50] X. Li and R. Yang, "Effect of lattice mismatch on phonon transmission and interface thermal conductance across dissimilar material interfaces," *Phys Rev B Condens Matter Mater Phys*, vol. 86, no. 5, Aug. 2012, doi: 10.1103/PhysRevB.86.054305.

[51] Z. Tian, K. Esfarjani, and G. Chen, "Enhancing phonon transmission across a Si/Ge interface by atomic roughness: First-principles study with the Green's function method," *Phys Rev B Condens Matter Mater Phys*, vol. 86, no. 23, Dec. 2012, doi: 10.1103/PhysRevB.86.235304.

[52] O. L. Anderson, "A SIMPLIFIED METHOD FOR CALCULATING THE DEBYE TEMPERATURE FROM ELASTIC CONSTANTS," 1963.

[53] F. H. Stillinger and T. A. %'eber, "Computer simulation of local order in condensed phases of silicon."

[54] S. Nosé, "A molecular dynamics method for simulations in the canonical ensemble," *Mol Phys*, vol. 52, no. 2, pp. 255–268, 1984, doi: 10.1080/00268978400101201.

[55] W. G. Hoover, "Canonical dynamics: Equilibrium phase-space distributions," 1985.

[56] B. Li, C. Zhang, B. Jiang, W. Han, and Z. Lin, "Flow-Enabled Self-Assembly of Large-Scale Aligned Nanowires," *Angewandte Chemie*, vol. 127, no. 14, pp. 4324–4328, Mar. 2015, doi: 10.1002/ange.201412388.

[57] C. M. Hangarter, Y. Rheem, B. Yoo, E. H. Yang, and N. v. Myung, "Hierarchical magnetic assembly of nanowires," *Nanotechnology*, vol. 18, no. 20, Apr. 2007, doi: 10.1088/0957-4484/18/20/205305.

[58] J. Yao, H. Yan, and C. M. Lieber, "A nanoscale combing technique for the large-scale assembly of highly aligned nanowires," *Nat Nanotechnol*, vol. 8, no. 5, pp. 329–335, 2013, doi: 10.1038/nnano.2013.55.